8.A.4 Nuclear Physics B30 (1971) 77-115 North-Holland Publishing Company

NEUTRON-PROTON ELASTIC SCATTERING FROM 5 TO 30 GeV/c *

Bruce G. GIBBARD **, Michael J. LONGO,
Lawrence W. JONES and John R. O'FALLON ***
University of Michigan, Ann Arbor, Michigan 48104

Michael N. KREISLER
Princeton University, Princeton, New Jersey 08540

Martin L. PERL
Stanford Linear Accelerator Center,
Stanford, California 94305

Received 1 February 1971

Abstract The differential cross section for neutron-proton elastic scattering was measured in the diffraction region with incident neutron momenta between 5 and 30 GeV/c. The experiment was an optical-spark-chamber–counter experiment conducted at the Brookhaven National Laboratory alternating gradient synchrotron. A well collimated neutron beam with a broad energy spectrum was incident on a liquid hydrogen target. The scattered neutrons were detected in a thick-plate spark-chamber array while the recoil protons were detected and momentum analyzed in a magnetic spectrometer with thin-foil spark chambers.

The results indicate that the neutron-proton cross sections are very similar to but not identical with the proton-proton cross sections. The diffraction peak in the neutron-proton system does show shrinkage with increasing incident momentum but exhibits no auxiliary structure.

1. INTRODUCTION

In 1964 our group carried out an experiment at the Bevatron to measure np differential cross sections over a large range of angles for neutron momenta up to 7 GeV/c [1]. The technique employed was unusual in that a neutron beam containing a broad range of neutron energies was used, and the incident neutron energy was determined from a kinematic reconstruction of each event. Some results of the Bevatron experiment are shown in fig. 1. [2] ‡.

* The work was supported by the US National Science Foundation and the US Atomic Energy Commission
** Now at CERN, Geneva, Switzerland.
*** Now at St Louis University, St. Louis, Missouri, 63103.
‡ See ref. [1] for a listing of references to np data available in 1969. Ref. [1] also contains a more complete discussion of theory and of some aspects of the experimental technique.

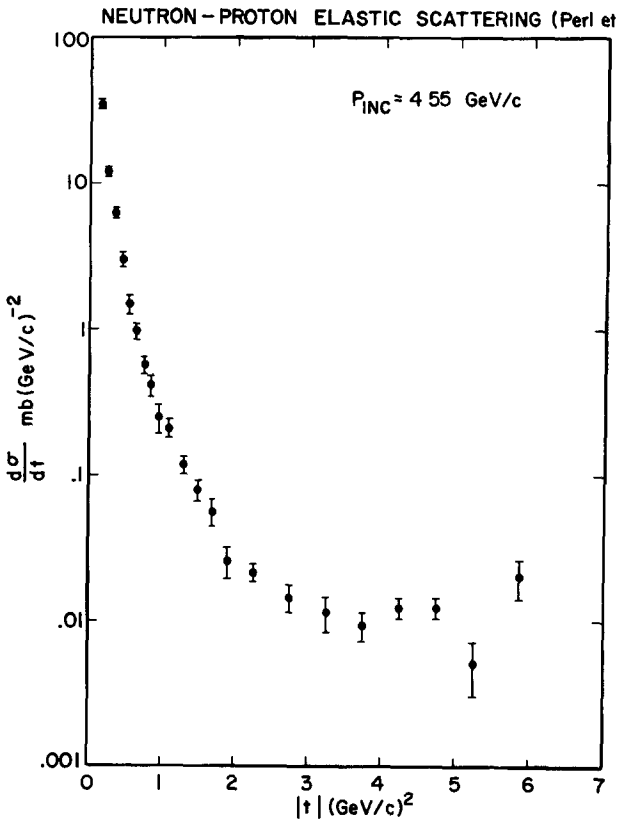

Fig 1. Neutron-proton differential cross section as a function of four-momentum transfer squared for 4 55 GeV/c incident momentum (from ref [1])

This report describes an experiment carries out at the Brookhaven AGS which made use of the same technique to measure np differential cross sections in the diffraction region for incident neutron momenta up to 30 GeV/c [3]. The purpose of this experiment was to investigate the shrinkage of the diffraction peak, to search for auxiliary structure near the peak, and, in general, to compare np forward elastic scattering with available pp data.

2. THEORETICAL PRELIMINARY: REGGE-POLE DESCRIPTION OF NN SCATTERING

For nucleon-nucleon interactions the contributing Regge trajectories are believed to be the P (Pomeranchuk), P'(f_0), ω, ρ, and A_2 (R) [4]. The relative way in which these poles contribute to various nucleon-nucleon

In addition to the neutrons in the beam, there were three possible contaminants. These were K^0, $\bar{n}$ and γ. On the basis of production cross sections, contamination from the $\bar{n}$ and the K^0 was estimated to be $< 2\%$ above 10 GeV/c [6]. Gammas, however, were more numerous. These were effectively removed by inserting 1.25 cm lead γ-filters in the beam at the upstream end of each of two of the sweeping magnets. These filters served to convert gammas to electron-positron pairs which could then be swept from the beam. The total of 2.5 cm of lead used removed $\approx 99\%$ of the incident gammas while stopping only 17% of the neutrons.

A study of the beam made by exposing Polaroid plates behind an aluminum converter plate showed that at the hydrogen target the beam diameter was approximately 3.3 cm with almost no surrounding halo. Fig. 3 shows Polaroid exposed 10 m downstream of the hydrogen target

Four monitor telescopes were used to monitor the relative intensity of the neutron beam. The M-monitor was a three-counter telescope located 4.5 m from the internal beryllium target (fig. 2). It measured the flux of charged particles coming from the beryllium target which was expected to be proportional to the neutron beam intensity. The L-monitor was a three-counter telescope which viewed the liquid-hydrogen target at an angle of 25^0 (Fig. 4). It was assumed that the number of charged particles produced

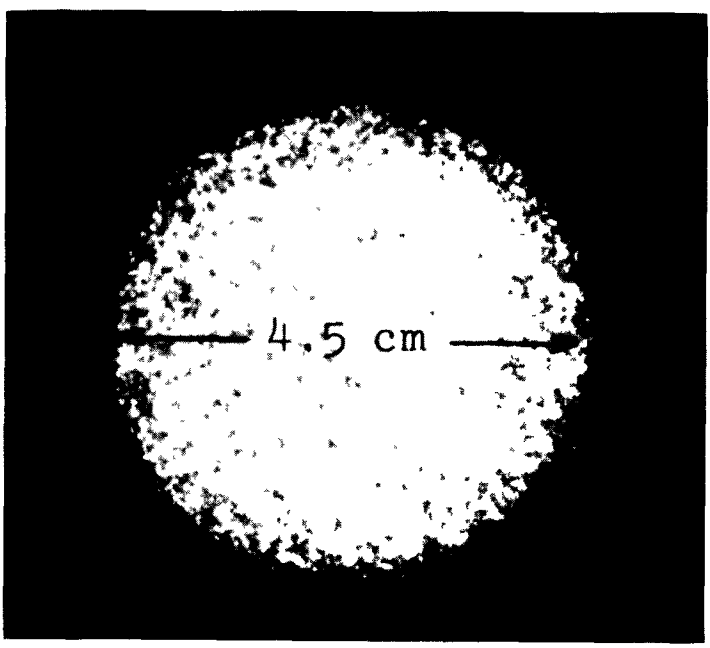

Fig. 3. An X-ray plate exposed to the neutron beam 10 m downstream of the hydrogen target. An image intensifier screen was used to produce this image. The sharp definition of the beam with negligible halo is well demonstrated.

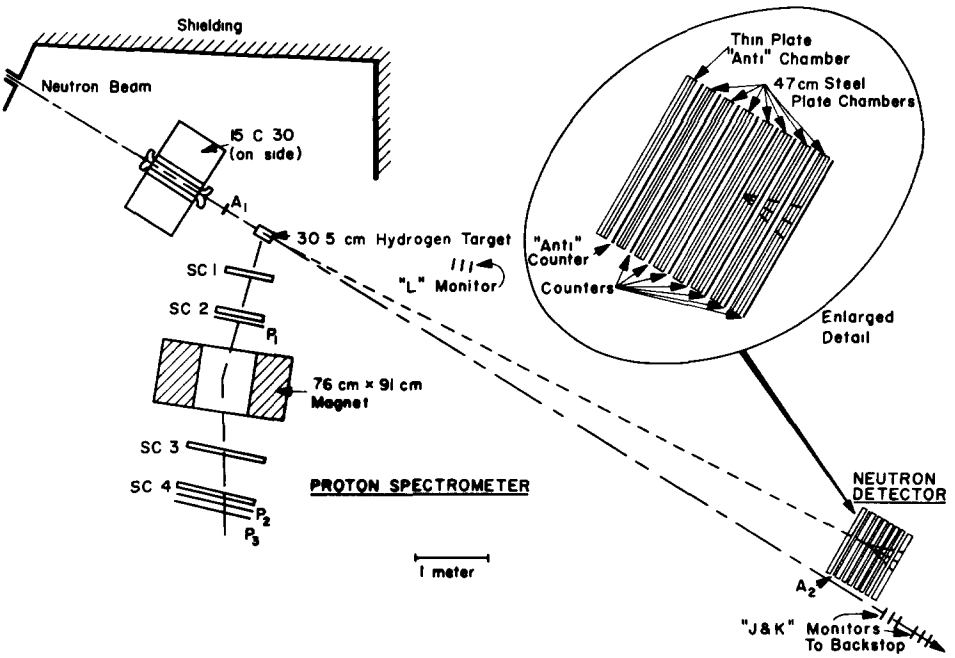

Fig 4. The layout of the apparatus in the experimental area.

in the hydrogen target was proportional to the beam intensity. Monitors J and K were three-counter telescopes, positioned directly in the neutron beam downstream of the rest of the experiment (fig. 4). The first of the three counters was used as an anticounter and the space between it and the second counter contained polyethylene which acted as a converter.

3.2. *Liquid-hydrogen target*

The liquid-hydrogen target flask was made of 0.025 cm mylar. It was 30.5 cm long and 6.35 cm in diameter. The target flask was enclosed in a 0.10 cm thick aluminum vacuum jacket. Located immediately in front of the hydrogen target was counter A_1. It was used as an anticounter to insure that no charged particle entering the hydrogen target could be responsible for a triggering event.

3.3. *Proton spectrometer*

The spark chambers used in the proton spectrometer were thin-plate, optical spark chambers with six 1 cm wide gaps each. The spark chambers were of two different sizes. Small ones whose active region was 56 cm by 15 cm were used in front of the magnet and are designated SC_1 and SC_2 in fig. 4. Larger chambers with an active region 107 cm by 34 cm were used behind the magnet and are designated SC_3 and SC_4 in fig. 4. The chambers were run from a spark-gap system which supplied a pulse of 11.5 kV. A 40 V dc clearing field was also employed. The plates of all the spark chambers were made with 0.025 mm aluminum foil.

elastic interactions can be found in the following manner. Let us suppose that the contribution to $\bar{p}p$ is as follows:

$$\bar{p}p \qquad P + f_0 + A_2 + \omega + \rho \ .$$

To change from the $\bar{p}p$ system to the pp system requires a charge conjugation so we must change the sign of those contributing poles which change sign under charge conjugation, the ω and ρ:

$$pp \qquad P + f_0 + A_2 - \omega - \rho \ .$$

To change from the pp to the np system requires an isospin change so we change the sign of those contributing poles possessing non-zero isospin, the ρ and A_2:

$$np \qquad P + f_0 - A_2 - \omega + \rho \ .$$

From these considerations it is possible to draw some simple conclusions. The difference between np and pp must be solely a result of the A_2 and ρ-contributions. Since the np and pp total cross sections have generally been found to be in good agreement, it is believed that the A_2 and ρ-contributions are quite small. The difference between the pp and $\bar{p}p$ is due to the ω- and ρ-trajectories. Since this difference has been observed to be large and since the ρ-contribution appears to be small, it is likely that the ω-contribution is substantial. We thus conclude that the np amplitude in the forward direction should be represented by substantial contributions from P, f_0, and ω and small contributions from A_2 and ρ.

A particularly simple result can be obtained in the high-energy limit. The amplitudes from all trajectories decrease with increasing energy more rapidly than the P. Thus at suffuciently high energy the P alone contributes so that if $\alpha_P(t)$ is the trajectory and $\beta_P(t)$ the residue of the P pole

$$\frac{d\sigma}{dt} = \frac{1}{16\pi s(s - 4m^2)} \beta_P^2 \left(\frac{s}{s_0}\right)^{2\alpha_P(t)} \ .$$

Here s is the square of the total energy in the c.m. and t is the square of the four-momentum transferred to the proton (in our metric t is always negative); also m is the nucleon mass.

Assuming that $s \gg 4m^2$ and, according to convention [4], setting $s_0 = 1\ (\mathrm{GeV}/c)^2$, we get:

$$\frac{d\sigma}{dt} \approx \frac{\beta_P^2}{16\pi} e^{2[\alpha_P(t)-1](\ln s)} \ .$$

If $\alpha_P(t)$ is taken to be linear in t, this formula can be used to explain the shrinkage observed in the pp data and in lower energy np data, where the term shrinkage is used to denote the increasing steepness of the diffraction peak with increasing energy. Recent results from Serpukhov indicate that in the pp interaction this shrinkage effect continues for momenta as high as 70 GeV/c [5]. We will later use such a parameterization to study the shrinkage in the data from this experiment.

3. EXPERIMENTAL DESIGN

In our experiment a well-collimated neutron beam with a broad energy spectrum struck a liquid-hydrogen target. The angle of the recoil proton and its momentum were determined in an optical spark-chamber spectrometer while the trajectory of the scattered neutron was determined from its interaction point in an array of steel-plate spark chambers and counters. The proton and neutron detectors were too small to cover the entire range of four-momentum transfers to be studied in one setting. The detectors were designed so that it was fairly easy to move them to different angular ranges. In the course of the experiment there were a total of four overlapping "settings" for the detectors.

3.1. *Beam*

The internal proton beam of the AGS, with an intensity of about 10^{12} protons per pulse, was accelerated to a momentum of 29.4 GeV/c. The beam was then spilled over a period of about 300 msec onto a beryllium target, 1 mm in diameter The neutron beam was taken off at an angle of 15 mrad with respect to the primary proton beam. The distance from the internal target to the liquid-hydrogen target was 49 2 m (fig. 2). The defining collimator was 2.54 cm in diameter and was located 34.7 m from the internal target. The other collimators were non-defining collimators used to reduce the halo around the beam.

Charged particles were removed from the beam by a series of sweeping magnets, the first of which was the AGS magnet itself. Two sweeping magnets located within the AGS tunnel were oriented so that they swept charged particles horizontally out of the beam. The final sweeping magnet, just before the hydrogen target, was oriented to act as a pitching magnet and thus swept charged particles up or down out of the horizontal plane, thereby minimizing background from charged particles in the spark chambers.

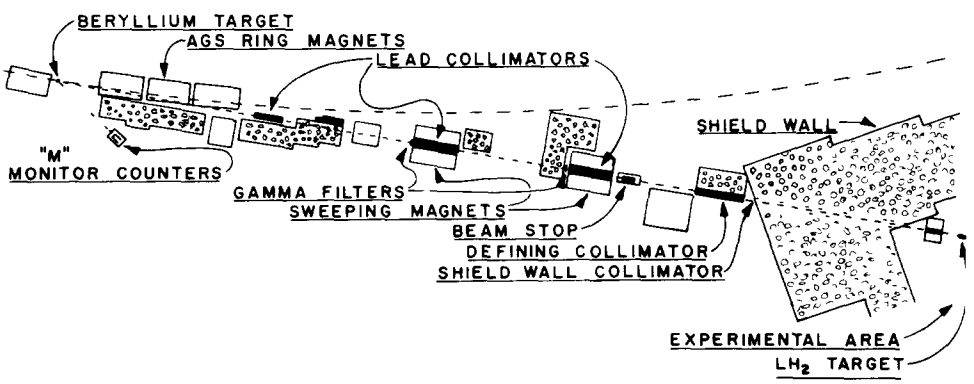

Fig 2. The arrangement of the neutral beam line.

The magnet used in the proton spectrometer, an "H" magnet with a 21.6 cm aperture 91 cm long, was run at three different currents corresponding to central field values of 4 kG for the first setting, 9 kG for the second setting, and 15 kG for the third and fourth settings of the proton spectrometer. At each current the field of the magnet was measured on a three-dimensional grid with an automatic mapper of the SLAC Magnetic Measurements Group to an accuracy better than 1%.

The magnet supported the entire spectrometer with the chambers, counters and camera all mounted in a superstructure solidly attached to it. The magnet itself was then mounted on a motorized carriage which traveled on a circular section of rails. Thus the position of the spectrometer could be easily changed from setting to setting as the experiment proceeded.

The event trigger included the requirement of a fast coincidence between counters P_1, P_2, and P_3 in the proton arm. The counter P_1, positioned immediately behind chamber SC_2 in fig. 4, was $0.6 \times 15 \times 53$ cm. Counters P_2 and P_3, positioned behind chamber SC_4, were $1.0 \times 34 \times 112$ cm. These counters were all made of Pilot B scintillator and were viewed by 6810A photomultipliers through lucite light pipes.

Pulsed luminescent panels [7] placed behind aluminum masks were used as fiducials for each view of each chamber. These luminescent panels were pulsed for 10 msec with a 400 V square wave at a frequency of 5 kHz just after the spark chamber fired and before the film was advanced.

In addition to the fiducials on each frame, there appeared a data box image. The data box contained a binary frame number, a decimal frame number, a roll number, and a rectangularly shaped master fiducial which was used with an automatic scanning system (see subsect. 5.2).

A 45° mirror was positioned at the end of each chamber so that on the film the stereo view appeared next to the corresponding direct view. The views of each chamber and the data box were carried by mirrors located above the magnet-spark chamber assembly (fig. 5) to the camera located at the downstream end of the spectrometer. The demagnification was approximately 40 : 1.

The camera employed on the proton arm, identical except for the lens to that used on the neutron arm, was a specially built 35 mm camera, holding 500 foot rolls of film and capable of taking up to 7 pictures in 300 msec [8]. Eastman Linagraph Shellburst film was used.

3.4. *Neutron detector*

The neutron spark chambers were thick-plate optical chambers. There were seven such chambers, each containing five 0.48 cm steel plates and four 0.95 cm gaps. The active volume of the neutron array was 122 cm wide, 28 cm high, and 97 cm deep. The array of chambers contained 130 g/cm^2 of steel which is $\approx$1.43 collision lengths [9]. Thus, about 76% of the neutrons passing through the array interacted. The chambers were fired by a spark gap supplying 15 kV pulses. They also had a 40 V dc clearing field. In front of the thick plate chamber array one thin plate spark chamber was used as an "antichamber". If a track was observed to have passed through this chamber, it was rejected during scanning. This served as a check on the anticounter A_2.

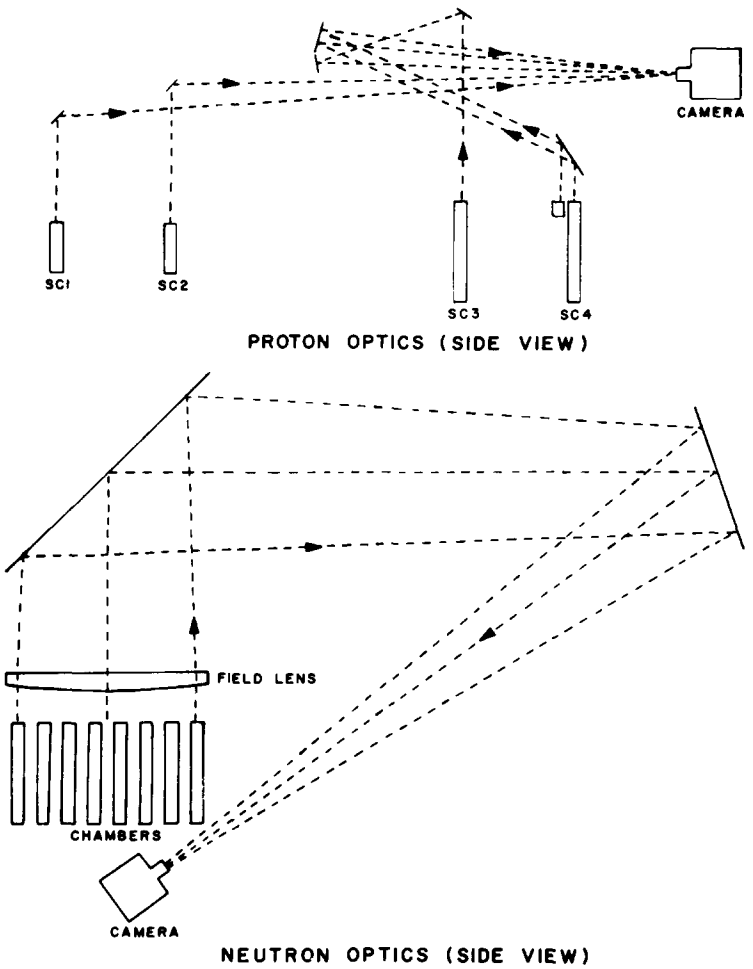

Fig. 5. Schematic view of the spark-chamber optics.

A scintillation counter was positioned behind each of the eight spark chambers. The counters were trapezoidal in shape, having a length of 119 cm. The end closer to the beam was 17.8 cm high while the other end was 29.5 cm high. They were viewed with 6810A photomultipliers. Part of the triggering requirement was that there be a coincidence between any two successive neutron counters with no vetoing signal from the anticounter A_2. This requirement was chosen to maximize the probability of finding a usable track in at least one of the chamber modules.

The same arrangement of luminescent panels and fiducial masks was used on the neutron arm that used on the proton arm. In addition, an identical data box was used. The binary counters on the proton and neutron data boxes were neon lamps wired in series to insure that they indicated identical numbers.

The direct view of the chambers passed through a field lens to an overhead mirror, as shown in fig. 5. A 45° mirror brought the stereo view through a small field lens and up to the same overhead mirror. From this mirror the paths went to a second mirror and then down to the camera positioned underneath the array.

The field lenses put the effective camera position at infinity and allowed the camera to look directly into every gap in the array.

3.5. *Electronics*

The fast electronics circuits used were primarily commercially made [10]. A schematic of the fast electronics is shown in fig. 6. The trigger for an event required a charged particle passing through the proton arm and a neutral particle entering the neutron detector forming one or more charged particles. The corresponding logical requirement was $P_1P_2P_3N_1N_{1+1}\bar{A}_1\bar{A}_2$,

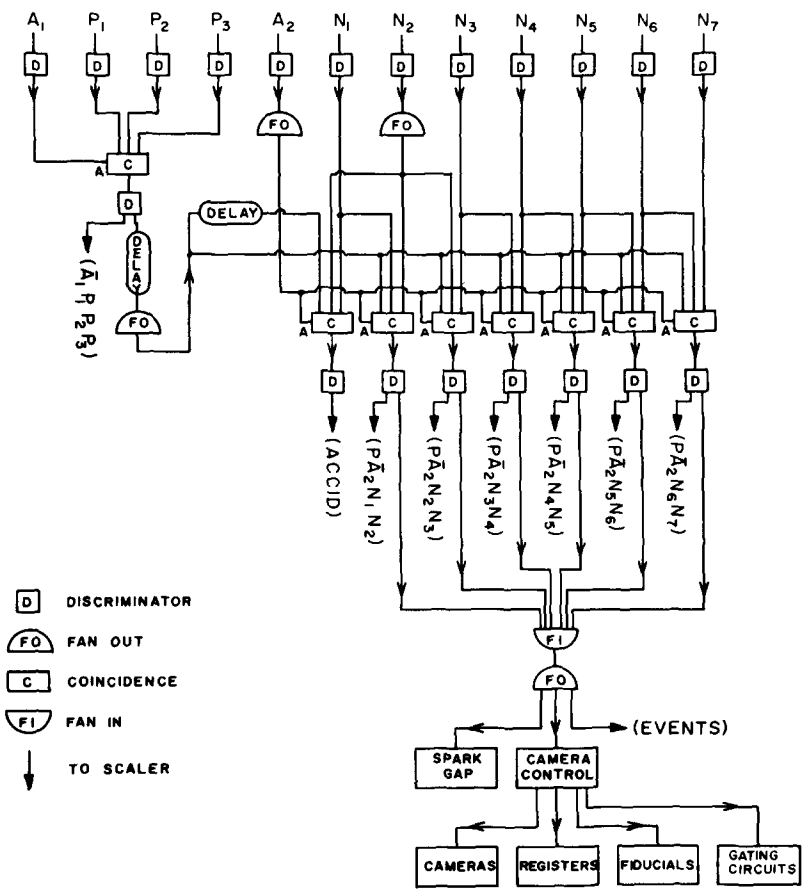

Fig. 6. Schematic of the electronic logic.

(a coincidence between the three counters in the proton arm with any two successive counters in the neutron detector and no vetoing pulse from either the anticounter positioned in front of the liquid-hydrogen target or the one before the neutron detector). The timing requirements in the logic were kept loose enough to insure that no elastic events were lost. In order to obtain an estimate of the accidentals for this signature, coincidences of the neutron trigger with proton triggers which were delayed long enough to insure that no actual correlation could exist were also scaled.

The entire fast logic was tested at least every 12 hours during the data taking by means of light pulsers attached to each scintillator. Timing cable lengths to the pulsers were adjusted so that the signals generated would simulate the timing of a typical elastic event.

In addition to the fast logic itself, certain gating logic was used, including a gate which could be triggered by the beam spill monitor. This gated off the entire system, including monitors, when the instantaneous beam rate was above a certain level. This substantially reduced accidental rates. Another gate was triggered after the detection of a good event which kept the fast logic inoperative until the slower elements such as the spark gaps and cameras were ready for another event.

4. DATA REDUCTION

4.1. *Neutron film*

The format of the neutron film can be seen in fig. 7. Neutrons entered the array from the right. The antichamber was positioned to the right of the rightmost column of fiducials. The scanners were instructed to measure all events which (1) contained a shower whose vertex was definitely within the chamber, (2) had no backward-going prongs, and (3) did not extend from the antichamber. Events containing sufficiently few and scattered sparks that no vertex could be determined were excluded. The scanner was instructed to measure each vertex if there were more than one that satisfied these criteria. The fitting program later tried each possibility to obtain the best fit. These criteria for the neutron vertices are essentially arbitrary since, as discussed below, the neutron detection efficiency does *not* affect the cross sections. The main reason for setting up the criteria was to improve the accuracy of the neutron vertex measurement and to make the yield of events as consistent as possible among the various scanners. A transparent plastic template with ruled rays originating from the crosshair of the measuring machine was used to aid the scanner in setting the crosshair on the vertex. A range of brackets around the measuring point aided the scanner in estimating the uncertainty in the vertex location measurement. This was recorded, along with a "type number" indicating the kind of event and its vertex definition. These were later used to assign uncertainties in the vertex location for each event.

All the neutron scanning and measuring was done on a focal plane digitizing machine which has a least count of 3.2×10^{-4} cm. This machine was connected via a Datex unit to a card punch. Twice a week a check of

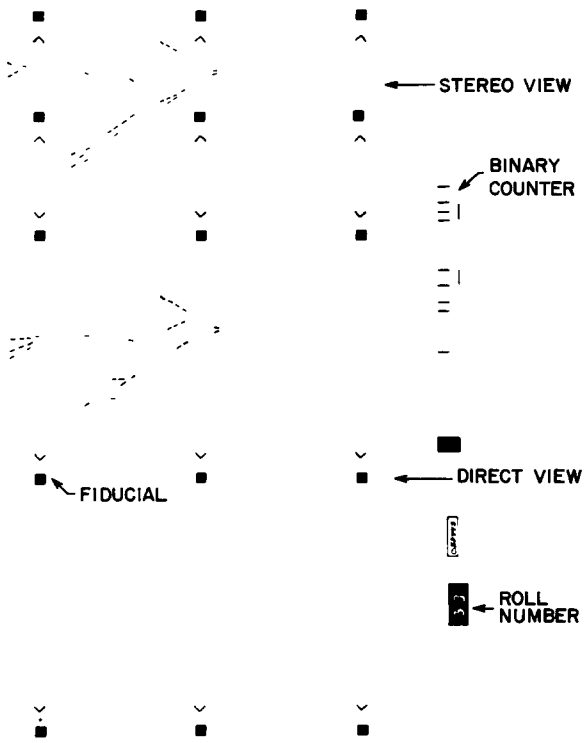

Fig. 7. Schematic of a typical neutron frame.

the scanning machine was made for reproducibility of measurements and for linearity of the axes.

The fraction of neutron events which were successfully measured was a function of the angle at which the neutron detector was set and was also, unfortunately, somewhat a function of the scanner. Typical measurable event yields for the neutron film ranged from 85% at the smallest angle setting to 61% at the largest. The actual fraction of elastic events as determined by the reconstruction program was much lower than this.

4.2. *Proton film*

The yields for the proton film were much higher than those of the neutron film, typically above 95%, and were neither as setting dependent nor as scanner dependent.

The Michigan Automatic Scanning System (MASS) [11] was used to scan most of the proton film. It measured events at a rate of approximately 3000 per hour. The precision and reliability of its measurements were significantly better than those of a hand-scanner. No attempt was made to

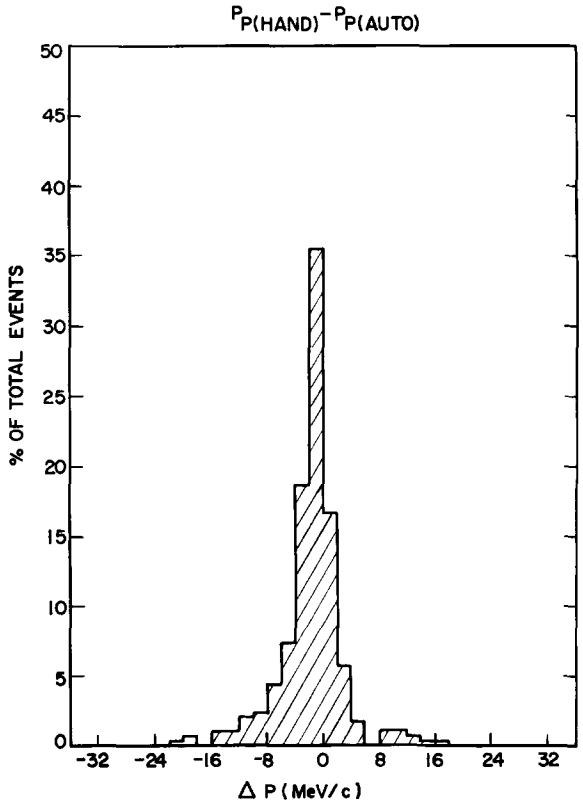

Fig. 8. Distribution of the differences between the proton momentum as determined by handscanning and by autoscanning. The very small systematic shift would have negligible effect on the data.

use MASS for the neutron pictures since the pattern recognition capability required to locate vertices accurately would have been very difficult to provide.

Of the 400 000 frames of proton film analyzed, 85 % were scanned by MASS. The yield of successfully interpreted proton frames for MASS was 95 % of that obtained by hand. The most significant checks of the performance of the autoscan system came from the final experimental values which it produced. In fig. 8 the differences between the hand and autoscan values obtained for the proton momentum are plotted against frequency of their occurence for a typical roll. The width at half maximum of the difference distribution is 5 MeV/c with the center of the distribution displaced from zero by 1 MeV/c. On the average there was a systematic shift of about 0.3 % between the hand and autoscan results for the proton momenta. Similarly, very small differences were encountered for other variables

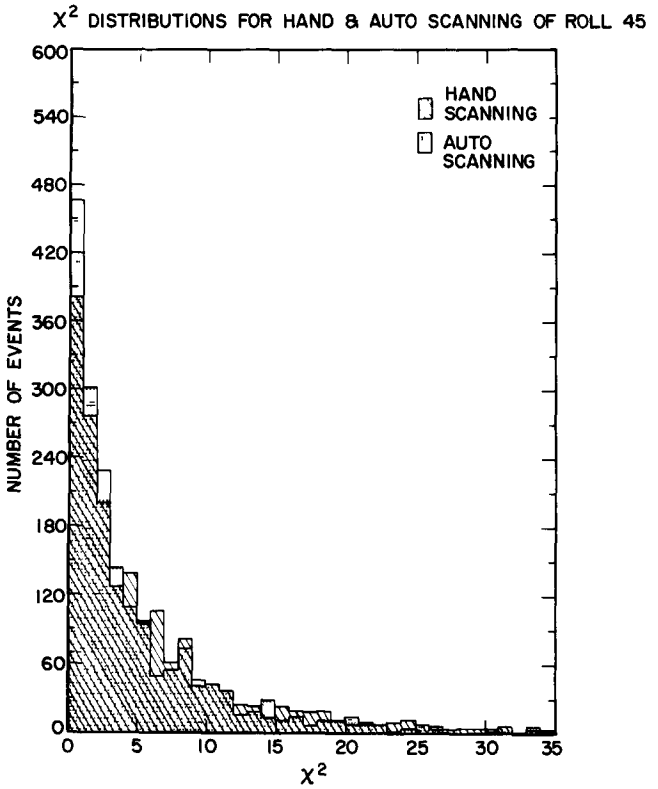

Fig. 9 Chi-square distributions for a roll of film as measured by hand and by autoscanner.

studied. The only quantity which showed a significant difference was the chi-square (see subsect. 5.1). Fig. 9 shows the χ^2 distributions for both the hand and the autoscanning of a roll. The average χ^2 of autoscan data was 2 less than that of the handscan. This is a reflection of the greater precision of the autoscanner measurements.

4.3. *Scaler data and bookkeeping*

The scaler data from the experiment were transferred to data processing cards, and computer checked for consistency between the various monitors. This check showed that the four monitors had typically tracked to 0.3 %.

The final step in the data reduction was executed by a matching program which took as input a binary tape reduction of neutron film scanner output and a binary tape reduction of proton film scanner output. It matched up frame numbers within a given roll, assigned the proper permutations of scanner interpretations within a given frame, and wrote a final output tape

record containing all of the information for a given frame that the reconstruction program would later need. The matching program also produced a summary for each roll of the scan yields and the multiplicity totals. These were compared for the various rolls of a given setting to detect rolls for which anomalous behavior of the chambers or scanners produced inconsistencies in the yield which might affect the results.

5. DATA ANALYSIS

5.1. *Event reconstruction*

The reconstruction of an event began with the determination of the real space locations of the sparks from the film coordinates. With the knowledge of the fiducial positions and the effective camera position, one can determine a three-dimensional real space line along which a spark is located for each view of each chamber. The final coordinates of the spark in a given chamber were obtained by determining the point of closest approach (nominally the intersection) of the two lines, one for each of the two views, direct and stereo, of that chamber. In the case of the neutron array, the three-dimensional location of the vertex of a shower was determined rather than the position of sparks.

For the proton spectrometer film, it was possible to make checks of the real-space transformations by studying "straight-throughs". These were pictures taken with the proton spectrometer with the normal triggering requirement, but for which the analyzing magnet was turned off. The paths of the undeflected particles were then projected forward from the first two chambers and backward from the last two chambers into counter P_1, which was the largest single source of multiple coulomb scattering. Distributions of the differences in vertical and horizontal angles as well as the differences in projected position were studied. Those distributions were centered about zero which indicated that the proton chamber positions were known accurately. The widths of these distributions were found to be consistent with that expected from multiple coulomb scattering.

Once the real space positions of the sparks and vertex were determined, it was possible to make a first check on the event. The path of the proton in the first two chambers was projected back toward the hydrogen target. The reconstruction program required that the proton path intersect the hydrogen target if reconstruction of the event was to continue. Since the neutron beam diameter was 3.3 cm while the target itself was 6.35 cm in diameter, this constraint was relatively loose and even strongly multiple coulomb scattered protons were seldom lost. The actual number of raw events cut by this check was less than 3 %.

The interaction point was taken to be the midpoint of the projected proton path in the hydrogen target. The angle of the scattered neutron was then determined by connecting the vertex in the neutron detector array to this interaction point in the hydrogen target.

The following procedure was used to determine the momentum of the proton from the four known points of its trajectory and the magnetic field

map: first, an estimate of the proton momentum was obtained using $\int B dl$ with the assumption of a uniform field; second, a point of intersection with counter P_1 was obtained by projection from spark chambers SC_2 and SC_2; third, the proton was traced back from SC_3 and SC_4 through the magnet to P_1. This was done by integrating stepwise through the magnet using the estimated momentum. If the intersection of the trace-back with counter P_1 was within 0.025 cm of the intersection from the front chamber projection, the momentum estimate was deemed to be correct. If the difference exceeded 0.025 cm, a correction to the estimated momentum was made and another trace-back was attempted. While as many as twenty trace-backs were permitted, the usual number required was four.

A substantial correction to the momentum as determined in the spectrometer had to be made, especially for lower proton momenta, because of the energy loss which the proton suffered as it passed through the liquid hydrogen, mylar, aluminum and air on the way from the interaction point through the spectrometer. The correction was made by interpolation in a set of range-energy tables [12].

Once the angle of both particles and the momentum of the proton were known, these variables were submitted to a fitting subroutine. The subroutine used was adapted from the Lawrence Radiation Laboratory program "GUTS" [13], and the description which follows parallels that in ref. [13]. The input to the fitting program included, in addition to the values of the measured quantities, a set of error estimates on the measured quantities which were used to compose an error matrix. The seven measured quantities for which entries existed in the error matrix were the two incident neutron angles, the two scattered neutron angles, the two recoil proton angles, and the recoil proton momentum.

The estimated errors on the incident neutron angles were determined by the collimator aperture. The error estimate for the scattered neutron vertex position depended primarily on the nature of the shower and the scanner's ability to interpret it. Thus the error estimate for each event was separately calculated to be the sum in quadrature of the scanner's own estimate of the uncertainty and a constant uncertainty of 0.64 cm. The primary contribution to the error in the determination of the proton angles and momentum came from the multiple coulomb scattering of the proton. Since this was momentum and path dependent, these error estimates were calculated separately for each event.

The variables used in the fitting program (historically suited to bubble-chamber measured quantities) were defined as follows:

$$\varphi = \varphi \ , \qquad K = P \sin\theta \ , \qquad S = \frac{1}{\tan\theta} \ ,$$

where θ is the angle made with the vertical and φ is the angle in a horizontal plane made with the incident neutron direction.

Calling the incident neutron particle 1, the target proton particle 2, the scattered neutron particle 3, and the recoil proton particle 4, one can express the four-momentum-energy equations as:

$$K_1 S_1 - K_3 S_3 - K_4 S_4 = 0 ,$$
$$K_1 \sin\varphi_1 - K_3 \sin\varphi_3 - K_4 \sin\varphi_4 = 0 ,$$
$$K_1 \cos\varphi_1 - K_3 \cos\varphi_3 - K_4 \cos\varphi_4 = 0 ,$$
$$E_1 + E_2 - E_3 - E_4 = 0 ,$$

with

$$E_i = [K_i^2(1+S_i^2) + m_i^2]^{\frac{1}{2}} ,$$

where m_i is the rest mass of the ith particle.

Of the variables in these four equations, only K_1 and K_3 are known. Since there are two unknowns and four constraining equations, this is a two-constraint fit. In what follows the measured values of these variables for each particle are referred to as x_i^m. The calculated values of the variables are x_i.

The error matrix

$$G_{ij}^{-1} = \delta x_i^m \, \delta x_j^m ,$$

is used to define the chi-square as

$$\chi^2 \equiv \sum_{ij} (x_i - x_i^m) \, G_{ij} (x_j - x_j^m) .$$

The error in the recoil-proton momentum depended primarily on the multiple coulomb scattering of the proton within the magnet gap. The error in the recoil-proton angle depended on the multiple coulomb scattering between the interaction point and the spectrometer while the error in the scattered neutron angle depended on the uncertainty in the location of the neutron vertex. Since to first order none of the errors depended upon the same things, it was not likely that there existed any strong correlations between the errors in the different quantities. If the errors are assumed to be uncorrelated the error matrix becomes diagonal, and

$$\chi^2 = \sum_i (x_i - x_i^m)^2 \, G_{ii} .$$

The constraint equations are of the form:

$$F_k(x_i) = 0 , \qquad k = 1 \ldots c .$$

Introducing Lagrange multipliers α_k, one can write:

$$\chi^2 = \sum_i (x_i - x_i^m)^2 \, G_{ij} + 2 \sum_k \alpha_k F_k(x_i) .$$

This is true because the second term on the right is known to be zero. It is now necessary to find the choices of x_i and α_k for which the χ^2 is minimum.

$$\frac{\partial(\chi^2)}{\partial x_j} = 2\sum_i (x_i - x_i^{\mathrm{m}})\, G_{ij} + 2\sum \alpha_k \frac{\partial F_k}{\partial x_j} = 0 \,, \tag{1a}$$

$$\frac{\partial(\chi^2)}{\partial \alpha_k} = 2F_k(x_i) = 0 \,. \tag{1b}$$

Eq. (1b) are exactly the original constraint equations. These nine simultaneous non-linear equations required a solution by numerical methods. The method employed utilized an assumed linearity over the region near x^{m} and produced the following iterative algorithm:

(1) $$F_\lambda^n = \left(\frac{\partial}{\partial x_i} F_\lambda\right)\Big|_{x_i = x_i^n} \,,$$

(2) $$E_{i\lambda}^n = \sum_j G_{ij}^{-1} F_{j\lambda}^n \,,$$

(3) $$H_{\lambda\mu}^n = \sum_j (E^n)_{\lambda j}^{\mathrm{T}} F_{j\mu}^n \,, \quad \text{where } (E^n)^{\mathrm{T}} \text{ is the transpose of } E^n \,,$$

(4) $$b_\lambda^n = F_\lambda^n + \sum_j (x_j^{\mathrm{m}} - x_j^n) F_{j\lambda}^n \,,$$

(5) $$\alpha_\lambda^{n+1} = \sum_\mu (H^n)_{\lambda\mu}^{-1} b_\mu^n \,,$$

(6) $$x_i^{n+1} = x_i^{\mathrm{m}} - \sum_\lambda E_{i\lambda}^n \alpha_\lambda^{n+1} \,.$$

For the first iteration:

$$x_i^0 = x_i^{\mathrm{m}} \quad \text{and} \quad \alpha_\lambda^0 = 0 \,.$$

In applying this procedure one need only take the appropriate partial derivatives of the constraint equations and then iterate until there is no significant improvement in the χ^2.

From the final fitted values of the fitting parameters, the more intuitive physical quantities, momentum and angle, were calculated. For each roll histograms of the incident neutron spectrum, recoil-proton spectrum, coordinates of interaction points, and χ^2 distributions were plotted and compared to check for inconsistencies.

5.2. *Monte Carlo*

A Monte-Carlo technique was used to calculate the geometric efficiency of the apparatus. For each setting of the apparatus, four-momentum transfer, and incident momentum, the Monte-Carlo program simulated a large number of events. It assigned appropriate random variation to quantities which in the actual experiment experienced random variations. Among

these quantities were the planar angle, the proton multiple coulomb scattering in the hydrogen target, the proton multiple coulomb scattering in the magnet traversal, the interaction point in the hydrogen target, the interaction point of the neutron as it passed through the neutron array, and the incident neutron angle.

In allowing for the effect of multiple coulomb scattering, the distribution of scattering angles was assumed to be Gaussian rather than the more appropriate Molière distribution [14]. The error introduced by this assumption in the final cross sections was small compared to statistical errors.

For this calculation the spatial distribution of the incident neutron beam was estimated from Polaroid pictures such as fig. 3. The attenuation of the neutron beam as it passed through the hydrogen target and the absorption of protons via strong interactions between the interaction point in the hydrogen target and the final counter in the proton arm were also taken into account.

Fig. 10 shows a typical plot of the detection efficiency (normalized to a fixed fraction of the total efficiency) as a function of the four-momentum transfer for one setting and for one incident energy. The cutoff in acceptance at small $|t|$ was a result of neutrons missing the edge of the neutron detection array closest to the neutron beam. The cutoff in acceptance at large $|t|$, somewhat more gradual, was a result of the protons missing the edge of the spectrometer closest to the beam; first those from only the downstream end of the hydrogen target were lost with more cut off as $|t|$

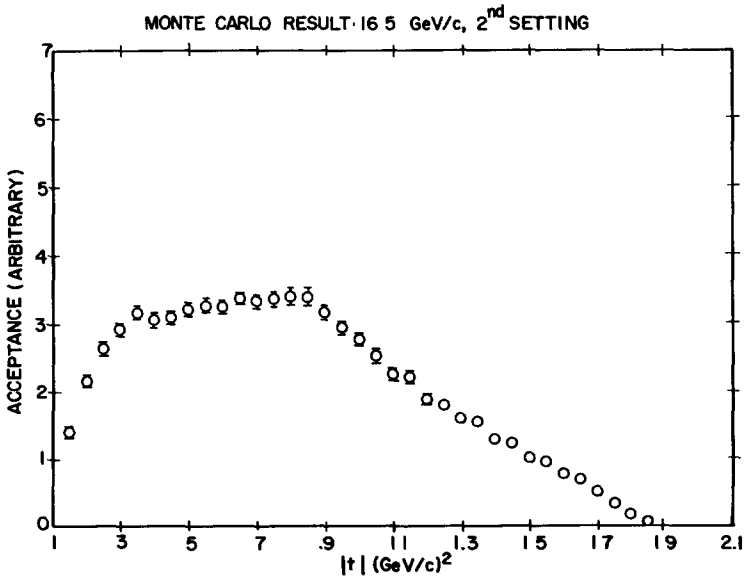

Fig. 10. Acceptance as a function of the four-momentum transfer squared (setting No. 2).

increased. Variations in the φ angle acceptance with $|t|$ for both detectors produced smaller variations on these dominant characteristics of the efficiency plots. The most serious types of uncertainties in the calculated efficiencies would be a result of uncertainties in the real space position of the apparatus. If these had been in error the apparatus might not have been sensitive in a area where the Monte-Carlo program indicated sensitivity which could cause large errors in the cross sections for certain ranges of and neutron momentum. In order to minimize problems resulting from measurement uncertainties, fiducial volumes smaller than the active volumes of the chambers and counters were defined. With these fiducial volumes errors could occur only if there were gross measurement errors (0.6 cm for the proton arm, 2 cm for the neutron arm). Errors of this magnitude would have been apparent in the results from the reconstruction program. Therefore it was assumed that the statistical error in the Monte-Carlo generated events represented the uncertainty in the calculated geometric efficiencies.

The efficiencies of the spark chambers and counters were assumed to be constant with t for the following reasons: In the proton spectrometer, care was taken to set the counter voltages well above threshold and to keep the timing requirements broad enough that there would be no momentum bias in triggering. Cases where the spark chambers appeared to fail as indicated by three tracks but no fourth one, were extremely rare, occuring less than 0.4% of the time. When failures did occur, there appeared to be no position or angle bias in the type of tracks which failed to register. A few rolls for which the chambers were functioning poorly were discarded.

For the neutron chamber array the most significant detector efficiency problem involved the efficiency with which scanners could determine vertices for showers. Positional biases were reduced by using only vertices away from the edges of the array where portions of the showers might be lost to view. An attempt was made to have each scanner scan rolls from each setting to minimize any t-dependence introduced by scanner efficiency. Rolls from different settings were alternated in the scanning sequence to minimize any effects from a slow change of efficiency with time.

The overall neutron detection efficiency was assumed to depend only on the neutron momentum and not on t. This will be discussed in subsect. 5.7. As can be seen from table 1, there was generally a large overlap in t between successive settings. Therefore an additional check on the variation with position in the efficiencies of the detectors was obtained by comparing results in the overlapping regions of the various settings. The agreement was very good and will be discussed when we consider relative normalizations. Table 1 also shows the range of acceptance in t for each setting and momentum range.

5.3. *Cross sections*

Final cross sections were produced by combining the following three sets of data: (1) the good events from the reconstruction program, (2) the geometric efficiencies for each of the four settings on an incident momenta grid of 2 GeV/c and on a four-momentum transfer squared grid of

Table 1
Range of acceptance in t as a function of setting and neutron incident momentum [$|t|_{max} = 2.10$ (GeV/c)^2].

Incident momentum range (GeV/c)	Acceptance range in $\|t\|$ (GeV/c)^2			
	setting 1	setting 2	setting 3	setting 4
	$63^\circ < \theta_p < 87^\circ$	$53^\circ < \theta_p < 77^\circ$	$42^\circ < \theta_p < 67^\circ$	$30^\circ < \theta_p < 56^\circ$
	$0.7^\circ < \theta_n < 7.3^\circ$	$0.7^\circ < \theta_n < 7\ 3^\circ$	$0.7^\circ < \theta_n < 7.3^\circ$	$3.1^\circ < \theta_n < 9.7^\circ$
5.4 - 9.4	0.10 - 0.50	0.10 - 1.00	0.30 - 0.50	1.25 - 1.45
9.4 - 13.4	0.10 - 0.65	0.10 - 1.50	0.35 - 1.60	1.35 - 2 10
13.4 - 17.4	0.10 - 0.70	0.10 - 1.60	0.35 - 2.10	1.50 - 2 10
17.4 - 21.4	0.15 - 0.70	0.15 - 1.70	0.40 - 2.10	1.60 - 2.10
21.4 - 25 4	0.20 - 0.75	0.25 - 1.75	0.40 - 2.10	1.95 - 2.10
25.4 - 29.4	0.30 - 0.75	0.30 - 1.75	0 40 - 2.10	

0.05 (GeV/c)^2, and (3) the monitor counter data for each roll which was used for normalization.

The data were processed one event at a time. The χ^2 was checked, and whenever it was greater than 15 (for two degrees of freedom) the event was rejected. Any event which had an incident neutron momentum outside the range $5.5 < P_{inc} < 30.5$ GeV/c or four-momentum transfer $|t| < 0.1$ (GeV/c)^2 was also rejected. For each event the detection efficiency was determined by interpolating from the table supplied by the Monte Carlo program. When the detection efficiency was greater than 60%, values for that event were added to appropriate bins in incident momentum and four-momentum transfer. Low efficiency events were rejected because the low efficiency implied that the event was near the edge of a detector and thus its probability of detection depended critically on our knowledge of the exact position of that edge. Since we did not know the positions of the edges with great accuracy, there were possibly large systematic errors in the detection efficiencies for these events and they were best discarded. When an event was accepted and binned, the reciprocal of the detection efficiency was added to a bin which was later used to determine the cross section value. The uncertainty in the cross sections was obtained by summing in quadrature the reciprocal of the square root of the number of events and the statistical uncertainty previously assigned to the detection efficiency values by the Monte Carlo program.

One additional correction was made to the data. Since events having a detection efficiency of less than 60% were rejected, the effective bin size of bins containing these events was reduced. There was also a bin size correction to be made simply because the bin size was increased for large t, as shown in table 2, in an attempt to compensate for the fact that so few events occured there. Actually, no events were detected above 1.7 (GeV/c)^2. The bin width corrections were made by dividing each bin value by the bin width.

All of the above calculations and corrections were done for each setting

Table 2
Bin width in t as a function of t.

$\|t\|$ range $(GeV/c)^2$	Bin width $(GeV/c)^2$
0.15 - 0 50	0 05
0.50 - 0 90	0 10
0.90 - 1 30	0 20
1 30 - 2 10	0 40

of the apparatus so that at this point there were four sets of cross sections, one for each setting. These then were combined to form one set of cross sections. This was done in a way that would minimize the effect on the cross sections of variations in the scanning efficiency. Within a given setting variations in neutron scanning efficiency as large as 25% were observed for different scanners. Since large numbers of scanners were used and all worked on rolls from all four settings, there was a great deal of

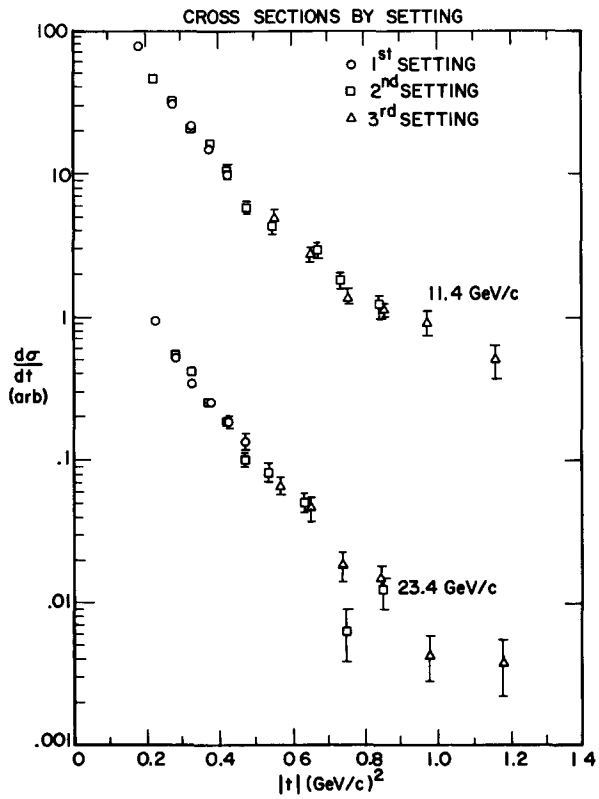

Fig 11. Differential cross section measurements at different settings for two incident momenta.

averaging out of the scanner efficiency variations. However there still remained a possibility that variations in scanner efficiencies might produce significant discrepancies in the relative normalization between different settings.

Since a scanner could not measure more good events on a roll than actually existed, an upper limit to scanner variation did exist. It was decided to select the three or four rolls with the highest yield out of the twenty to twenty-five rolls per setting and to regard these as having a uniform scanning efficiency for the four settings. All other rolls at a given setting were then normalized to give the same yield of good events/monitor as these.

The cross sections derived by this technique varied only slightly, generally within errors, from those derived assuming an averaging our of efficiencies. The agreement from setting to setting in the overlap region, while good in both cases, seemed somewhat better with the select roll normalization and so the select roll normalization was used. In fig. 11 the data for two incident momentum ranges for each of the three settings are compared. The agreement is quite good in the overlap region.

5.4. *Corrections*

In the computation of cross sections, only events with χ^2 less than 15 from rolls with the target full were used. To obtain the target-empty correction, the same procedure was used for the target-empty rolls. Since all cross sections were calculated on the basis of events per monitor, the cross sections produced by processing the target-empty rolls were exactly the contributions made to the actual cross sections by interactions occurring in the target flask and jacket which simulated good events. These values were thus the target-empty subtraction. Their value was always less than 1% of the measured cross section.

The correction for inelastics was somewhat larger and more complex. Cross sections were calculated for events with χ^2 between 30 and 55 (instead of 0 to 15 used for normal calculations). The cross sections for the χ^2 range 30 to 55 were intended to represent the contribution of inelastics simulating good events in the measured cross sections. This estimate of the inelastic correction was obtained from plots such as fig. 12. If a linear dependence of the background with χ^2 is assumed, the area under the line for χ^2 between 0 and 15 is approximately equal to the area between 30 and 55. This procedure assumes that the background does not peak up at small χ^2. It is difficult to justify this assumption except on the intuitive grounds that the background is composed of inelastic events which would not be expected to agree with the kinematics of elastic scattering as would be required to give a strong peak at small χ^2. More specifically, since most inelastics would have three or more body final states, for every coincidentally coplanar inelastic with a small χ^2 one would expect to see a number of non-coplanar inelastics contributing to large χ^2. The magnitude of the inelastic subtraction ranged from 1.4 ± 0.3% at small $|t|$ to 29 ± 11% at large $|t|$. The uncertainties in these subtractions are statistical.

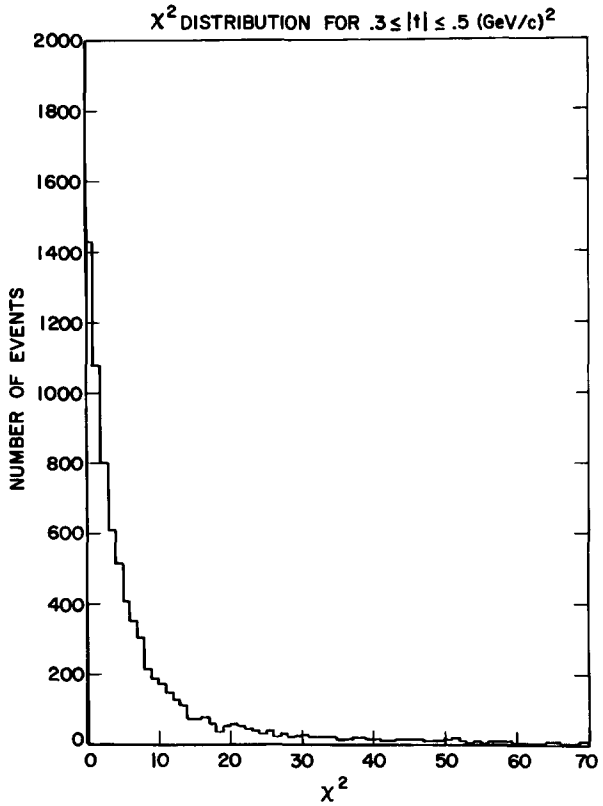

Fig. 12. Typical χ^2 distribution for a region in t containing a relatively low inelastic contamination.

5.5. *Checks*

A shower produced by a γ in the neutron spark chamber array could simulate a neutron shower. While it was believed that the showers produced were somewhat different, no effort was made to discriminate against the gammas during scanning. Since the contamination of the beam by gammas was never really determined and the analysis was not very sensitive to the incident particle mass, there could possibly be a contamination of the data by the reaction $\gamma p \rightarrow \gamma p$. In order to check for this reaction and at the same time to check for all other reactions which resulted in a γ triggering the neutron chambers, we used the following method: Each of the seven neutron chambers constituted about 1.3 radiation lengths but only about 0.2 nuclear mean free paths. Therefore, gammas were much more likely to give only the neutrons whose vertices were detected in the first spark chamber. If there were a γ contamination, the contamination should have been over 100 times as great in the first chamber as in the fourth chamber. Since the

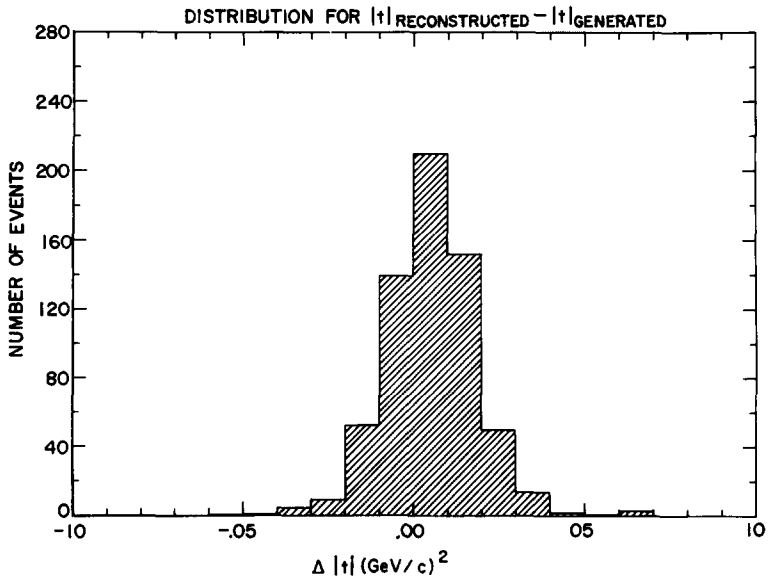

Fig. 13. Distribution of the difference between the four-momentum transfer squared of a Monte-Carlo generated event and the reconstructed values of the four-momentum transfer squared.

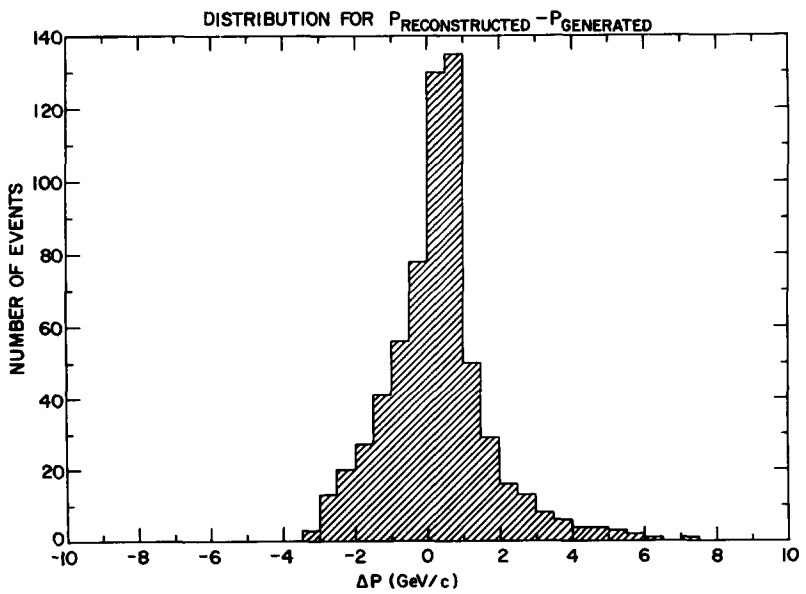

Fig. 14. Distribution of the difference between the incident momenta of Monte-Carlo generated events and the reconstructed value of the incident momenta.

cross sections based on the first chamber events were within errors the same as the overall cross sections, it was concluded that inelastic contamination involving a γ in the neutron array were not affecting the final data. This also served as a check that the cross sections were independent of the overall efficiency of the neutron detector.

Another very important check was made by generating simulated events with the Monte-Carlo program and them feeding the real-space spark location for these events into the reconstruction program. This involved assuming a definite incident neutron momentum and four-momentum transfer for the event. The kinematics of the event are then smeared out by coulomb scattering, etc. If the neutron momentum and four-momentum returned by the reconstructed program agreed well with the original values, it indicated that both the Monte Carlo and reconstruction programs were functioning properly. The results of this check are shown in figs. 13 and 14. In addition this procedure gave an estimate of the uncertainties with which the four-momentum transfer squared and the incident neutron momentum were determined (next section).

5.6. *Uncertainty estimates*

A comprehensive study of the uncertainties in the calculated values of the incident neutron momentum and t was made using the Monte-Carlo program. For a given P_{inc} and t the corresponding measured quantities were calculated. These quantities were then each separately perturbed by the estimated uncertainty in that quantity and the P_{inc} and t recalculated. The errors in P_{inc} and t resulting from the perturbation of the neutron scattering angle, proton recoil angle, and proton recoil momentum were combined in quadrature to produce the expected uncertainty in P_{inc} and t.

This study indicated that the uncertainty in t was essentially independent of t and P_{inc}, remaining constant at ± 0.017 $(\mathrm{GeV}/c)^2$. The uncertainty of P_{inc} was strongly a function of both t and P_{inc} and is shown in fig. 15. It is interesting to note that at large incident momenta and small t, the uncertainty becomes very large. The size of the P_{inc} bins was chosen with this in mind.

Another estimate of the uncertainty of the incident energy determination was obtained by studying the raw event neutron spectrum as shown in fig. 16. If one assumes that the spillover beyond 29.4 GeV/c, the AGS primary beam energy, in this spectrum was caused by Gaussian uncertainties in a function linearly dropping to zero at 29.4 GeV/c, then the standard deviation of this uncertainty which must be chosen to fit the data is ± 2.5 GeV/c. Calculated estimates of the uncertainties generally agreed with the observed uncertainties.

5.7. *Absolute normalization*

There was no way to do an absolute normalization internal to this experiment since the absolute number of neutrons in the beam and their momentum distribution were unknown. The normalization was done by fitting the data to the zero-degree point determined from the optical theorem and existing data on the real part of the np forward scattering ampli-

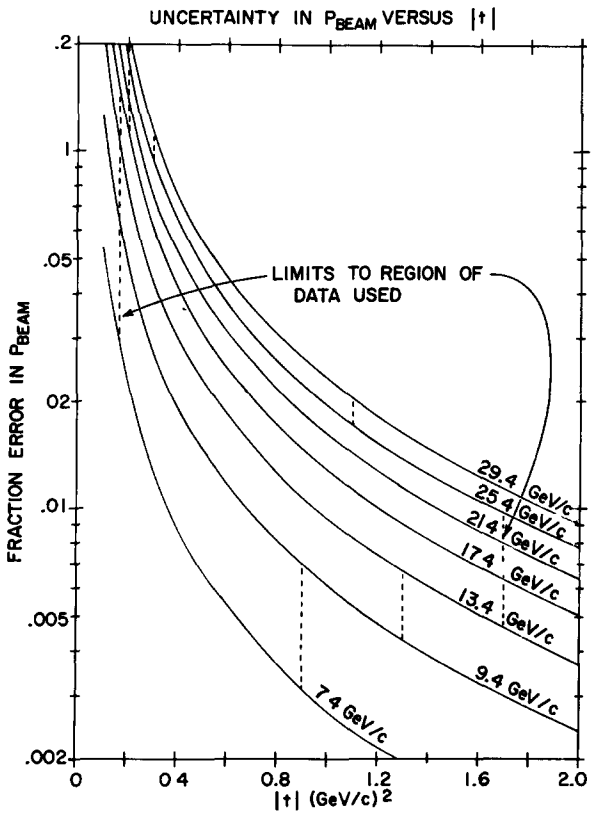

Fig. 15 The uncertainty in the incident neutron momentum as a function of the incident momentum and the four-momentum transfer squared.

tude. Each incident momentum range was independently normalized by this method. As well as removing the need for knowing the properties of the incident neutron beam, this approach allowed us to obtain results with only a general knowledge of the response of the neutron detector. It was necessary only that the detection efficiency be slowly varying with neutron momentum. For a given incident momentum the difference in the momentum of the scattered neutrons over the range of t studied was less than 0.9 GeV/c. A significant change in detection efficiency over such a small momentum range would have been extremely unlikely since the efficiency was simply related to the probability of a neutron interacting in steel. The data available indicate that the total nucleon-nucleon cross sections vary quite slowly with momentum and, furthermore, the Fermi motion of the nucleons in the iron would wash out any structure which might exist.

The cross section at $t = 0$ was obtained from the expression [1]

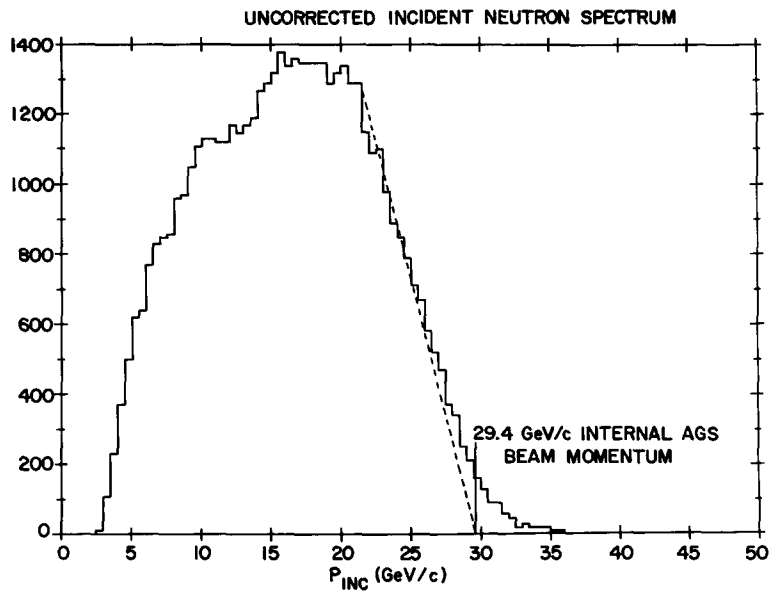

Fig. 16. The incident neutron spectrum without correction for detection efficiency

$$\left.\frac{d\sigma}{d|t|}\right|_{t=0} = \frac{1}{16\pi}\sigma_T^2(1+\rho^2) ,$$

where σ_T is the np total cross section and ρ the ratio of the real to the imaginary part of the forward scattering amplitude. As discussed in ref. [1], this neglects the spin-dependent amplitude.

The value for σ_T (the total neutron-proton cross section) used was 38 mb [15]. The values used for ρ (the ratio of the real to the imaginary part of the scattering amplitude) were obtained from experiments by Bellettini et al. [16] and Dalkazhov et al. [17]. A linear variation of ρ with P_{inc} was assumed with $\rho = -0.33$ near 20 GeV/c and $\rho = -0.45$ near 5 GeV/c.

The normalization was done in the following way: A linear fit in $\ln(d\sigma/dt)$ versus $|t|$ was made for the data with $|t| \leq 0.5$ (GeV/c)^2. The point of intersection of this line with the $t = 0$ axis was calculated for each incident momentum range. The factor required to shift the intercept to the optical-theorem points was then calculated. This factor was then used to multiply each point and uncertainty in that incident momentum range to obtain properly normalized data. The uncertainty in normalization is primarily due to uncertainties in σ_T and ρ, both of which are substantial. There is also some question as to the adequacy of a linear fit to the data for $t \leq 0.5$.

A resonable estimate of the uncertainty in normalization is $\pm 12\%$. The quoted cross sections can easily be corrected when better data are available. The values of ρ and σ_T used are given with the results for $d\sigma/dt$ in table 3.

Table 3
Differential cross sections.

7.4 ± 2.0 GeV/c		11.4 ± 2.0 GeV/c		15.4 ± 2.0 GeV/c	
$\lvert t \rvert$ (GeV/c)^2	$\frac{d\sigma}{dt}$ mb · (GeV/c)$^{-2}$	$\lvert t \rvert$ (GeV/c)^2	$\frac{d\sigma}{dt}$ mb · (GeV/c)$^{-2}$	$\lvert t \rvert$ (GeV/c)^2	$\frac{d\sigma}{dt}$ mb · (GeV/c)$^{-2}$
0.174	26.8 ± 0.80	0.175	24.7 ± 0.55	0.175	23.6 ± 0.49
0.223	18.8 ± 0.60	0.224	18.2 ± 0.50	0.223	16.1 ± 0.44
0.274	12.5 ± 0.50	0.274	12.5 ± 0.41	0.273	11.4 ± 0.36
0.323	9 99 ± 0.46	0.323	8.46 ± 0.34	0.323	8.51 ± 0.31
0.372	6.94 ± 0.40	0.374	6.29 ± 0.30	0.373	5.86 ± 0.26
0.423	4.50 ± 0 33	0.422	4.12 ± 0.26	0.423	3.65 ± 0.21
0.473	3.13 ± 0.34	0.474	3.05 ± 0.23	0.474	2.49 ± 0.18
0.538	3.17 ± 0.28	0.545	2.15 ± 0.16	0.549	1.76 ± 0.13
0.649	1.41 ± 0.21	0.651	0.941 ± 0.10	0.649	0.633 ± 0.080
0.743	0.931 ± 0.17	0.744	0.502 ± 0.075	0.745	0.335 ± 0.055
0.851	0.515 ± 0.13	0.846	0.360 ± 0.065	0.846	0.146 ± 0.038
0.934	0.253 ± 0.085	0.974	0.204 ± 0.055	0.969	0.639 ± 0.013
		1.170	0.0812 ± 0.025	1.197	0.0119 ± 0.0066
		1.476	0.0399 ± 0.014	1.515	0.0213 ± 0.0089
σ_T = 38 mb		σ_T = 38 mb		σ_T = 38 mb	
ρ = −0.42		ρ = −0.39		ρ = −0.36	

Table 3 (continued)

19.4 ± 2.0 GeV/c		23.4 ± 2.0 GeV/c		27.4 ± 2.0 GeV/c	
$\|t\|$ (GeV/c)^2	$\frac{d\sigma}{dt}$ mb · (GeV/c)$^{-2}$	$\|t\|$ (GeV/c)^2	$\frac{d\sigma}{dt}$ mb · (GeV/c)$^{-2}$	$\|t\|$ (GeV/c)^2	$\frac{d\sigma}{dt}$ mb · (GeV/c)$^{-2}$
0.223	16.4 ± 0.44	0.227	12.6 ± 0.45		
0.274	11.0 ± 0.35	0.273	7.08 ± 0.26		
0.323	7.33 ± 0.29	0.324	4 98 ± 0.21	0.325	5.11 ± 0.36
0.374	5.41 ± 0.25	0.373	3.27 ± 0.17	0.373	3.25 ± 0.26
0.423	3.97 ± 0.22	0.422	2 33 ± 0.15	0.422	2.31 ± 0.23
0.473	2.64 ± 0.18	0.474	1.48 ± 0.12	0.472	1.45 ± 0.13
0.550	1.26 ± 0.12	0.550	0.779 ± 0.080	0.553	1.00 ± 0.14
0.638	0.701 ± 0.080	0.650	0.445 ± 0.060	0.651	0.413 ± 0.085
0.743	0.363 ± 0.055	0.743	0.0778 ± 0.021	0.738	0.0685 ± 0.014
0.851	0.163 ± 0.038	0.848	0.1190 ± 0.028	0.881	0.0131 ± 0.0095
0.985	0.0684 ± 0.022	0.982	0.0170 ± 0.0095		
1.201	0.0339 ± 0.014	1.185	0.0127 ± 0.0060		
1.638	0.0023 ± 0.0029				
σ_T = 38 mb		σ_T = 38 mb		σ_T = 38 mb	
ρ = -0.33		ρ = -0.30		ρ = -0.27	

6. RESULTS

6.1. *Incident neutron spectrum*

Each incident-neutron energy range was independently normalized such that the following equation represents the relation of the observed cross section at $t = 0$ to that calculated at $t = 0$ using the optical theorem.

$$\left.\frac{d\sigma}{dt}\right|_{t=0}^{\text{observed}} \propto \left.\frac{d\sigma}{dt}\right|_{t=0}^{\text{optical point}} N_n E_{\text{Monte}} E_{\text{neu}} ,$$

where N_n is the neutron flux, E_{Monte} is the geometric efficiency and E_{neu} is the neutron detection efficiency. We then assumed that the neutron detection efficiency was independent of the neutron momentum, which should be a good assumption for all but the lowest energies, and derived the following equation:

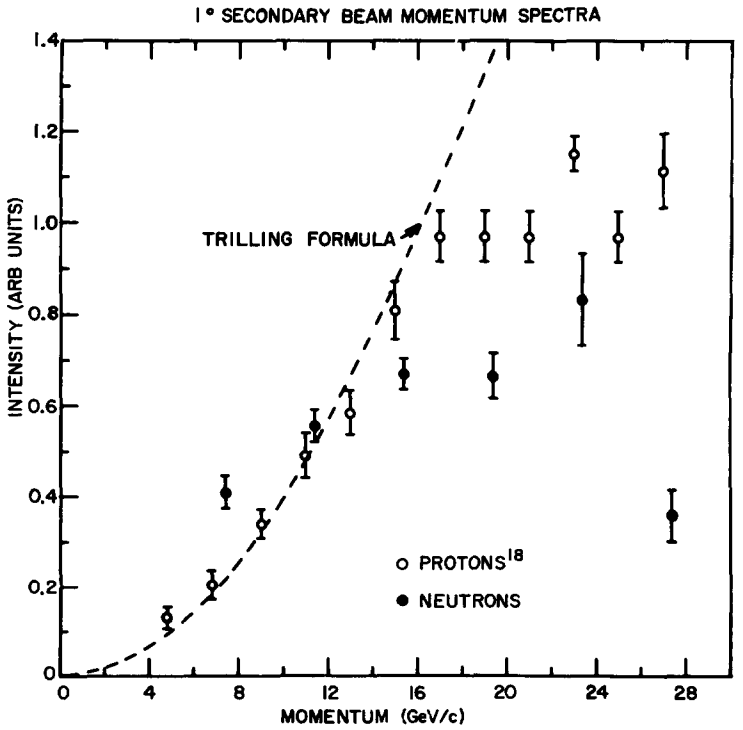

Fig 17. Comparison of our secondary neutron beam spectrum to a secondary proton beam spectrum and the Trilling parameterization for secondary proton beams.

$$N_n \propto \frac{\left.\frac{d\sigma}{dt}\right|_{t=0}}{\left.\frac{d\sigma}{dt}\right|_{t=0}} \frac{\text{observed}}{E_{\text{Monte}}}.$$

optical point

This gave us a measure of the incident neutron spectrum. In fig. 17 the spectrum, as determined by this method, is shown along with a comparable secondary proton spectrum [18] and a prediction obtained by using the Trilling fit [19] to data for inelastic proton production from a hydrogen target (as adapted to a beryllium target). Trilling's expression is

$$\frac{d^2N}{dPd\Omega} = P^2\left[1+0.47\frac{P_B}{P^2}\right]\left[\frac{0.56}{P_B}+\frac{0.44}{P_B^2}P\left(1-\frac{0.47P_B}{P^2}\right)\right] e^{[-3.0(P\theta)2]}.$$

In our case the primary beam momentum P_B was 29.4 GeV/c and the angle with respect to the incident beam θ was 0.85°. This equation gave the form of the rising portion of the spectrum only. Our neutron spectrum does not agree well with the proton spectrum or the Trilling parameterization.

6.2. *Cross sections*

In figs. 18 and 19 are plotted our cross sections which appear in tabular form in table 3 along with the values of σ_T and ρ used in the normalization. These data represent 22 500 elastic scatters obtained from 350 000 pairs of frames of film. The errors assigned to the values include: (1) statistical errors in the measurements, (2) errors in the determination of the detection efficiency, (3) errors in the target-empty subtraction and (4) errors in the inelastic background correction.

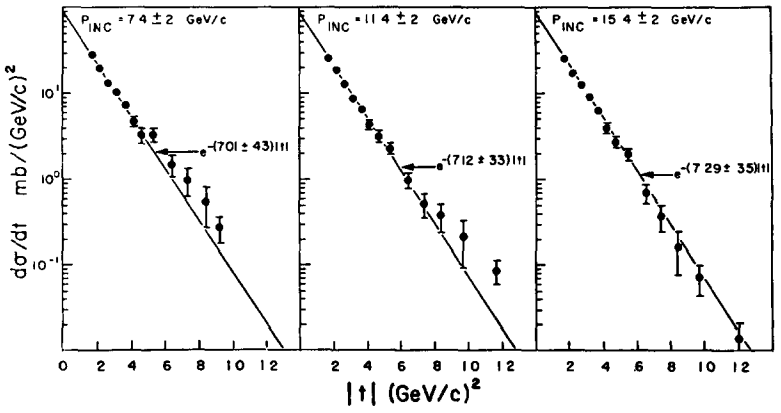

Fig. 18. Neutron-proton elastic scattering differential cross sections with exponential fit for $|t| < 0.5$ (GeV/c)^2.

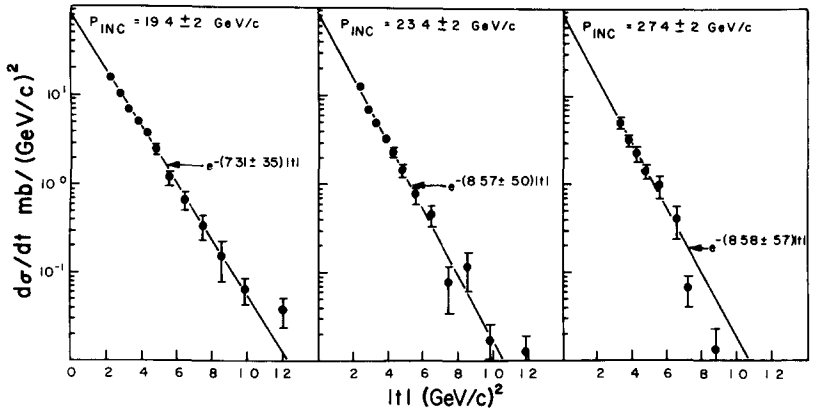

Fig. 19. Neutron-proton elastic scattering differential cross sections with exponential fit for $|t| < 0.5$ (GeV/c)^2,

The exponential curve which appears in the plots is a fit to $Ae^{-b|t|}$ for data points with $|t| < 0.5$ (GeV/c)^2. These curves fit well in this region and the $t = 0$ intercept is well determined. The $t = 0$ projections of these curves were used to obtain the absolute normalizations as discussed earlier. Uncertainties in normalization have not been included in the error assignments.

The cross sections in all cases drop smoothly with increasing $|t|$ and show no structure aside from the diffraction peak. In looking at the slope of the diffraction peak, there is some indication that it is steeper at higher incident momenta. At the lowest momenta there is a distinct curvature to the plots; this is not apparent at the higher momenta in the t-range studied.

6.3. *Fits and comparisons to other data*

The most often quoted fit applied to differential cross section data in the diffraction region is:

Table 4
Parameters of the fit of the experimental data to $Ae^{-b|t|}$.

P_{inc} (GeV/c)	b (GeV/c)$^{-2}$	χ^2	Degrees of freedom
7.4 ± 2.0	7.01 ± 0.43	4.4	5
11 4 ± 2.0	7.12 ± 0.33	3.6	5
15.4 ± 2.0	7.29 ± 0.35	6.8	5
19.4 ± 2.0	7.31 ± 0.35	4.0	4
23.4 ± 2.0	8.57 ± 0.53	15 2	4
27.4 ± 2.0	8.58 ± 0.62	4.4	2

$$\frac{d\sigma}{dt} = Ae^{-b|t|} .$$

These fits are shown in figs. 18 and 19. The fitted values of b are tabulated in table 4. The fits are generally good and the trend toward steeper slopes of the diffraction peak with increasing incident momentum is apparent. No explanation for the poor fit in the 23.4 ± 2.0 GeV/c bin is known.

It is interesting to compare our data with the proton-proton data and the lower-energy neutron-proton data. Measurements in the diffraction region for proton-proton scattering have been made by a number of groups over a wide range of energies. Measurements in the diffraction region for neutron-proton scattering have been made up to 7 GeV/c at the Bevatron [1] and up to 17 GeV/c at the CERN Proton Synchrotron [20]. Fig. 20 shows the fitted values of the parameter b. Solid symbols are used for the neutron-proton system including our experiment, and open symbols are used for the proton-proton system. All data were fitted with the same fitting program for values of $|t|$ less than 0.5 (GeV/c)^2 except the CERN data [20]. For these data there were insufficient points below 0.5 (GeV/c)^2 to allow a fit so the authors' own values for the slope were used which included points out to $|t|$ = 0.8 (GeV/c)^2 in the fit. There is some indication that this may cause the slopes to appear to be somewhat less steep than when smaller t-values are used, especially at lower beam momenta. The recent Serpukhov data [5] indicated by the dashed line are for very small t and are reported to have systematic uncertainties of approximately ± 0.5. Nevertheless these data are still significant in indicating a trend for the parameter b to increase with P_{inc} at higher energies in the proton-proton system.

Our data agree well with the low and intermediate momentum neutron-proton data. However there is some indication that the neutron-proton slopes are less than the proton-proton slopes above 6 GeV/c. The differ-

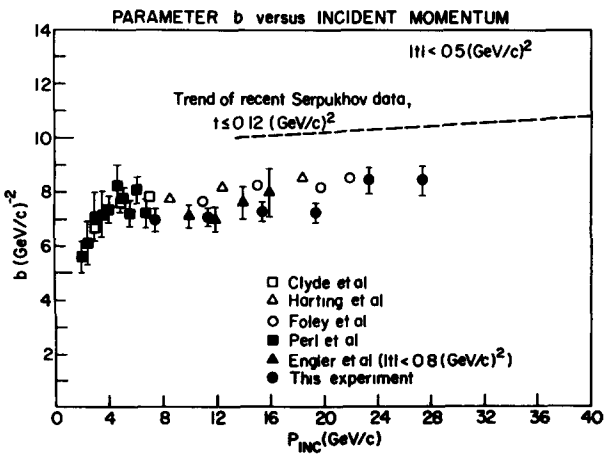

Fig. 20. The b parameter obtained by fitting the data to $e^{-b|t|}$.

ence is small, no more than two standard deviations at any point, but there does seem to be a dip at 6 GeV/c in the neutron-proton parameter after which it remains below the proton-proton values. Both sets of slopes do run parallel after the dip indicating comparable shrinkage of the diffraction peak.

A more transparent parametrization in which to study shrinkage is the expression suggested by the one Regge pole model discussed earlier in sect. 2,

$$\frac{d\sigma}{dt} = f(t)\, e^{2[\alpha(t)-1][\ln s]}$$

$$= f(t)\, s^{2(\alpha_0-1)}\, s^{2\alpha_1 t},$$

where $f(t) = [\beta p(t)]^2/(16\pi)$ and $\alpha p(t)$ is taken to be linear in t, $\alpha p = \alpha_0 + \alpha_1 t$. Here s, the c.m. energy squared, is in $(\mathrm{GeV}/c)^2$, that is, the Regge parameter conventionally called s_0 has been taken to be 1.0 $(\mathrm{GeV}/c)^2$.

The actual fit was made in the following manner. For each t-range, a value for α was obtained using the data for the six different values of incident momenta. In fig. 21 are plotted the values obtained for α as a function of the t-range used. We see that a linear fit to these points is not unreasonable. The fit was rather poor with a χ^2 of 41 for 7 degrees of freedom. The function obtained for α was:

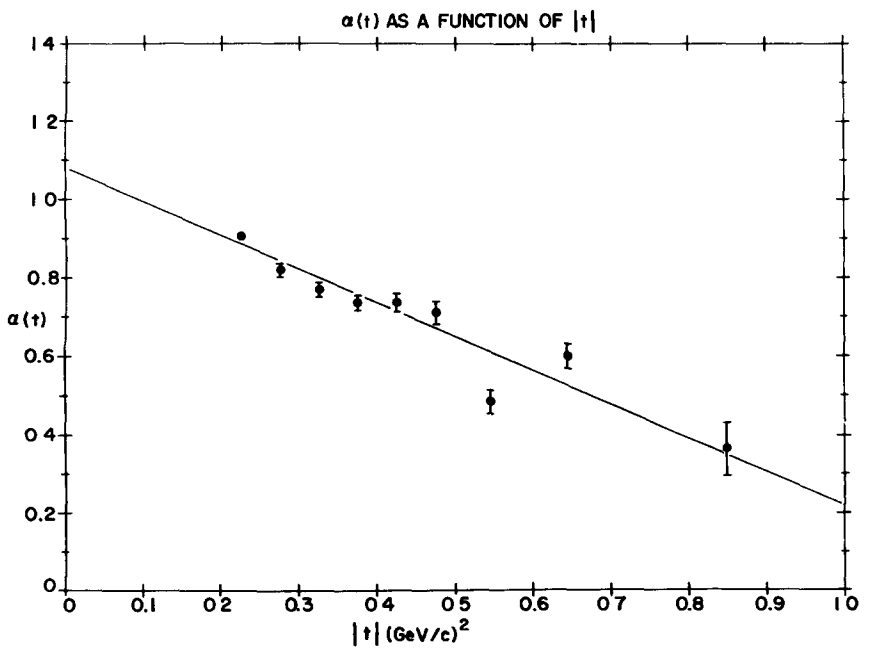

Fig. 21. Values of $\alpha(t)$ as a function of t obtained from fits to the data.

$$\text{np} \quad \alpha(t) = (1.08 \pm 0.05) - (0.86 \pm 0.14)\,|t| \ .$$

The negative coefficient of the linear term in $|t|$ indicates that there is shrinkage. Let us look at values obtained for the function α for other elastic scattering reactions:

$$\text{pp} \quad \alpha(t) = (1.05 \pm 0.02) - (0.69 \pm 0.05)\,|t| \ , \quad \text{(ref. [23])}$$

$$\bar{\text{p}}\text{p} \quad \alpha(t) = (0.90 \pm 0.08) + (0.91 \pm 0.38)\,|t| \ , \quad \text{(ref. [23])}$$

$$\pi^+\text{p} \quad \alpha(t) = (0.94 \pm 0.02) - (0.10 \pm 0.07)\,|t| \ , \quad \text{(ref. [24])}$$

$$\pi^-\text{p} \quad \alpha(t) = (0.98 \pm 0.03) + (0.06 \pm 0.07)\,|t| \ , \quad \text{(ref. [23])}$$

$$\text{K}^+\text{p} \quad \alpha(t) = (1.06 \pm 0.07) - (0.50 \pm 0.16)\,|t| \ , \quad \text{(ref. [25])}$$

$$\text{K}^-\text{p} \quad \alpha(t) = (1.00 \pm 0.14) + (0.39 \pm 0.32)\,|t| \ . \quad \text{(ref. [23])}$$

If one studies the $\alpha(t)$ of these various interactions, one notices the striking similarity between the proton-proton $\alpha(t)$ and the $\alpha(t)$ obtained for the neutron-proton system. A negative α_1 term corresponds to a diffraction peak which shrinks in width with increasing energy. Thus both nucleon-nucleon systems show shrinkage. The interpretation of $\alpha(t)$ for the meson-nucleon and nucleon-antinucleon systems is not so straightforward [27]. The proton-antiproton system shows antishrinkage; that is, the diffraction peak slope decreases with increasing energy. But for this system data exist only up to 12 GeV/c. The pion-nucleon system, with present data up to 20 GeV/c, shows neither shrinkage nor antishrinkage; the slope in constant with energy. The K^-p system may show a slight antishrinkage in the range of 10 to 18 GeV/c, but the data is poor. Finally the K^+p system shows shrinkage below 15 GeV/c; there is no data above 15 GeV/c. Therefore only the proton-proton and neutron-proton systems show clear shrinkage in the momentum range above 10 GeV/c.

In fig. 22 we compare neutron-proton cross sections at two momenta with proton-proton cross sections at comparable momenta. The cross sections have all been normalized to the same value at $t = 0$ so the plot is intended only to describe the relative shape. The behavior of the neutron-proton data is in general agreement with the proton-proton data.

One of the most interesting aspects of the proton-proton data is the distinct break which occurs in the 19 GeV/c data at a $|t|$ of about 1.2 (GeV/c)^2. Unfortunately our data are not good enough in that t-region to make any statement about a similar break in the neutron-proton data.

An additional parameterization which has been quite successfully applied by Krisch to the proton-proton system consists of regarding $\mathrm{d}\sigma/\mathrm{d}t$ as a function of $\beta^2 P_\perp^2$ (ref. [28]) where $P_\perp$ is the component of transferred momentum perpendicular to the incident momentum and β is the proton velocity in the c.m. The functional form actually employed by Krisch was:

$$\frac{\mathrm{d}\sigma}{\mathrm{d}t} = A_1 \mathrm{e}^{B_1\beta^2 P_\perp^2} + A_2 \mathrm{e}^{B_2\beta^2 P_\perp^2} + A_3 \mathrm{e}^{B_3\beta^2 P_\perp^2} \ .$$

This parameterization gives a good fit to most of the proton-proton data at energies above 3 GeV.

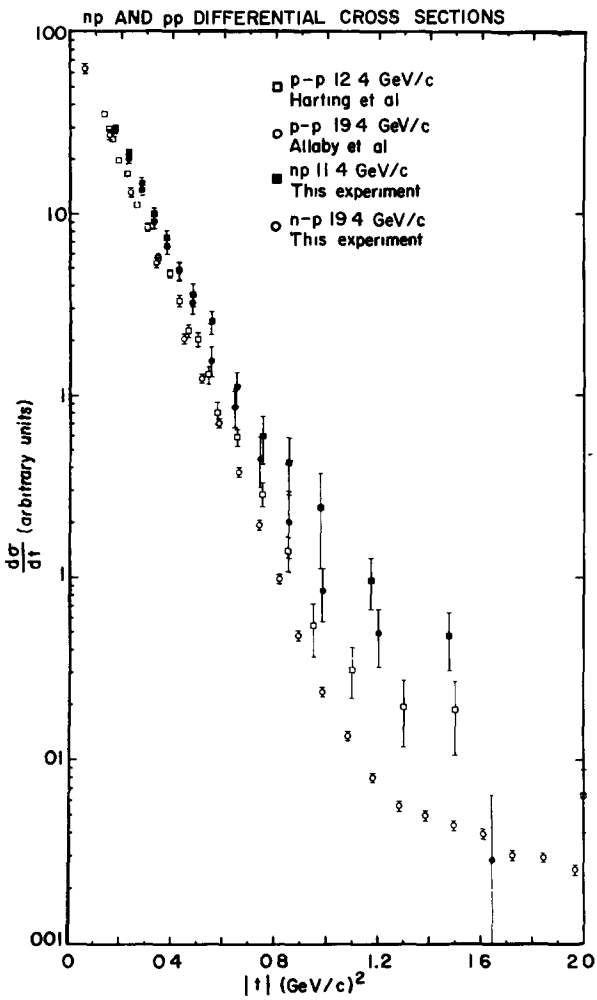

Fig. 22. The np and pp cross sections at comparable energies.

Before applying this fit to the neutron-proton data, there are two aspects of the parameterization which are worth mentioning. First, in this parameterization the differential cross sections at $t = 0$ ($\beta^2 P_1^2 = 0$) are independent of the incident energy. In view of the slowly varying total cross section and the optical theorem, this is only approximately true. Second, an ambiguity exists in the application of this parameterization to the neutron-proton system. In the proton-proton system there is, by virtue of particle identity, no backward scattering; in the neutron-proton system where the particles are not identical, backward scattering occurs. For

some values of $\beta^2 P_\perp^2$, there are two different values of the cross section, one corresponding to the backward hemisphere and the other to the forward hemisphere. For this reason when we apply this to neutron-proton data, we will limit ourselves to the forward scattering region.

The presently available neutron-proton data are only adequate to allow a fit in two exponentials. The result of applying this fit to the neutron-proton data is shown in fig. 23. A reasonable fit, the solid line in fig. 23, can be obtained for the low momentum neutron-proton data from the Bevatron [1]

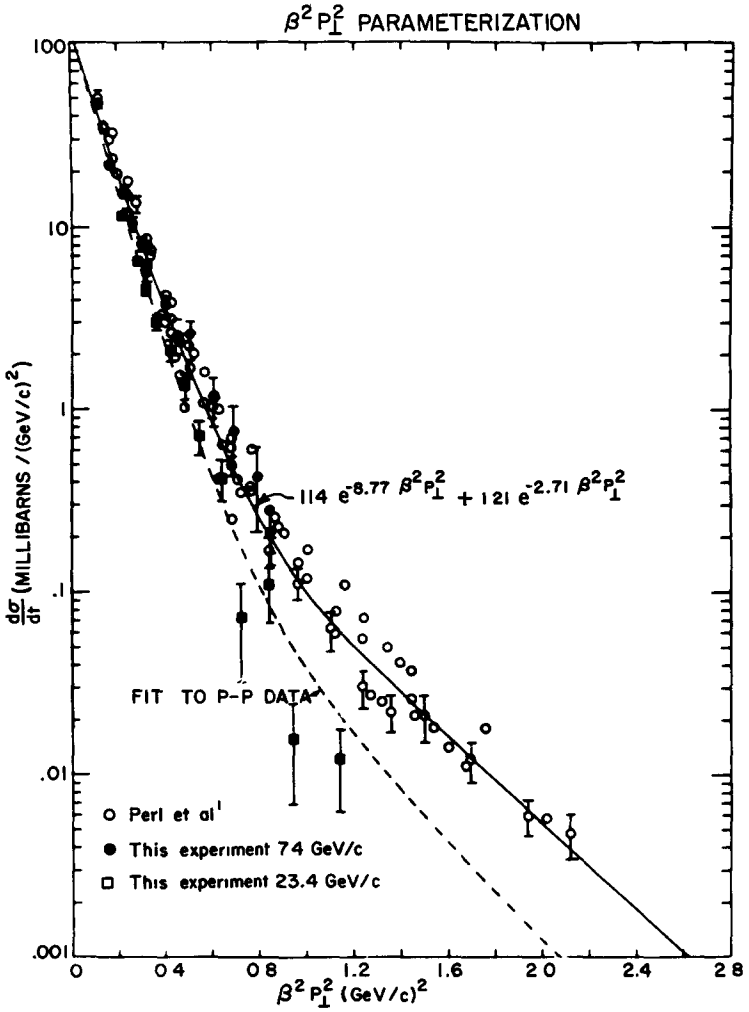

Fig. 23. Neutron-proton cross sections plotted against $\beta^2 P_\perp^2$ and the curve for the fit obtained for the proton-proton data in this parameterization.

which agree with the lowest momentum set of our data. The fit obtained is definitely less steep than obtained for the proton-proton data. This is consistent with the generally smaller values of the b parameter observed earlier. The higher momentum neutron-proton data are found to fall significantly below the curve and, in fact, appear to fall more nearly on the proton-proton line than the low momentum neutron-proton data, as can be seen in fig. 23. We conclude that this parameterization does not fit the neutron-proton data as well as the proton-proton data.

6.4. *Conclusions*

The results of this experiment indicate that the neutron-proton differential cross section is characterized by a smoothly falling diffraction peak without auxiliary structure. The forward peak definitely does show shrinkage. The neutron-proton and proton-proton cross sections are, in general, very similar but do show one noticeable difference. This difference consists of a somewhat less steep diffraction slope for the neutron-proton system than for the proton-proton system from 6 GeV/c out to at least 20 GeV/c. Above 20 GeV/c the data no longer indicate a difference in the slopes.

J. Cox and W. T. Toner made many important contributions to this experiment, especially in the setup and data-taking phase.

The assistance of J. Sanford, W. Merkle, and the entire A. G. S. staff is gratefully acknowledged. We also appreciate the assistance of G. DeMeester, O. Haas, S. T. Powell, III, R. Seefred, J. Smith, and S. Wilson during the setting up procedure.

For their help with the Automatic Scanning System, we would like to thank K. Fauser and P. Berneis; for their aid during the data analysis, we wish to thank B. Thompson, M. Follebout, R. Whitney, and J. Barnes.

REFERENCES

[1] M L Perl, J Cox, M J Longo and M N Kreisler, Phys Rev D1 (1970) 1857
[2] See ref [1]
[3] A preliminary report of the data from this experiment appeared in B G Gibbard, L. W. Jones, M J. Longo, J. R O'Fallon, J Cox, M. L. Perl, W T. Toner, M N Kreisler, Phys Rev Letters 24 (1970) 22,
See also B G Gibbard, thesis, Report UM-HE-70-11, Randall Laboratory of Physics, University of Michigan, Ann Arbor, Michigan 48104
[4] See, for example G Hite, Rev Mod. Phys. 41 (1969) 669;
V D. Barger and D. B. Cline, Phenomenological theories of high energy scattering (Benjamin, New York, 1969).
[5] G G Beznogikh, A. Buyak, K I Iovchev, N K. Zhidkov, L F Kirillova, P K Markov, B. A Morozov, V. A. Nikitin, S B Nurushev, P V. Nomokonov, M G Shafranova, V A Sviridov, V L. Solovianov, Truong Bien, V. I Zayachki and L. S Zolin, Phys Letters 30B (1969) 274
[6] S O. Holmgren, S. Nilsson, T Olhede and N Yamdagni, Nuovo Cimento 51A (1967) 305,
J. Barktke, W. A. Cooper, B. Czapp, H. Filthuth, Y. Goldschmidt-Clermont, L. Montanet, D R. O. Morrison, S. Nilsson, Ch Peyrou, R. Sosnowski, A. Bigi, R. Carrara, C Franzinetti and I. Manelli, Nuovo Cimento 29 (1963) 8.

[7] A. Barna, M N. Kreisler and M J Longo, Rev. Sci, Instr. 37 (1966) 521.
[8] D E Damouth and O E Haas, A pulsed rapid advance camera, Technical report no. 13, The University of Michigan, Ann Arbor, Michigan, 1963, unpublished.
[9] L. W. Jones, M. J. Longo, J O'Fallon and M N. Kreisler, Phys Letters 27B (1968) 328.
[10] R Sugarman, F C Merritt and W A. Higinbotham, Nanosecond counter circuit manual, BNL-711 (T-248), Brookhaven National Laboratory, Upton, L. I., New York, 1962
[11] A. Saulys, D I. Meyer and R. Allen, Nucl. Instr. Meth. 39 (1966) 335
[12] W H Barkas and M J. Berger, Table of energy losses and range of heavy charged particles, Report No. NASA SP-3013, 1964.
[13] J. P. Berge, "GUTS", Alvarez Group Memo 86, UCID-1251, University of California, Berkeley, California, January 19, 1960.
[14] D. M. Ritson, Techniques of high energy physics (Interscience Publishers, New York, 1961)
[15] M. N Kreisler, L. W. Jones, M J. Longo and J R O'Fallon, Phys. Rev. Letters 20 (1968) 468,
T. McCorriston, L W. Jones, M J. Longo, E. F. Parker, S. T Powell and M. N. Kreisler, submitted to XVth Int. Conf. on high energy physics, Kiev 1970.
[16] G. Bellettini, G. Cocconi, A N. Diddens, E. Lillethun, G. Matthiae, J. P. Scanlon and A. M Wetherell, Phys. Letters 19 (1965) 341.
[17] N. Dalkhazav, P A. Devinski, V I. Zayachki, Z. M. Zlatanov, L S Zolin, L. F Kirillova, Z. Korbel, P. K Markov, Ngo Kuang Zui, Nguyen Din Ty, V A Nikitin, L Rob, V. A. Sviridov, D. Tuvdendorzh, L. G. Khristov, Kh. M. Chernev, Chyong Byen and M G. Shafranova, Soviet J.Nucl. Phys. 8 (1969) 196.
[18] E W Anderson, E. J Bleser, G B Collins, T. Fujii, J Menes, F. Turkot, R A. Carrigan, R M Edelstein, N C. Hien, T J. McMahon and I Nadelhaft, Phys Rev. Letters 19 (1967) 198
[19] 200 BeV Accelerator Design Study, vol 1, Section XIII-1.3, p XIII-6, Lawrence Radiation Laboratory, University of California, Berkeley, California, 1965.
[20] J. Engler, K Horn, J. König, F Mönnig, P Schludecker, H. Schopper, P. Sievers, H Ullrich and K. Runge, Phys Letters 29B (1969) 321.
J König, thesis, Institut für Experimentelle Kernphysik, Universität Karlsruhe, Karlsruhe, Germany.
[21] A R. Clyde, thesis, Report No. UCRL-16275, Lawrence Radiation Laboratory, University of California, Berkeley, California, 1966
[22] D Harting, P Blackall, B. Elsner, A C. Helmholz, W. C. Middelkoop, B. Powell, B. Zacharov, P. Zanella, P. Dalpiaz, M N Focacci, S. Focardi, G. Giacomelli, L. Monari, J A. Beaney, R. A. Donald, P. Mason, L. W. Jones and D. O. Caldwell, Nuovo Cimento, 38 (1965) 60.
[23] K. J. Foley, R S. Gilmore, S. J. Lindenbaum, W. A. Love, S. Ozaki, E. H Willen, R. Yamada and L. C L. Yuan, Phys. Rev. Letters 15 (1965) 45.
[24] K. J. Foley, S. J. Lindenbaum, W. A. Love, S. Ozaki, J J. Russell and L. C. L. Yuan, Phys. Rev Letters 11 (1963) 425
[25] K. J Foley, S. J. Lindenbaum, W A. Love, S. Ozaki, J J. Russell and L. C L. Yuan, Phys. Rev. Letters 11 (1963) 503.
[26] J. V. Allaby, F. Binon, A. N. Diddens, P. Duteil, A Klovning, R. Meunier, J P. Peigneux, E J. Sacharidis, K. Schlüpmann, M. Spighel, J P. Stroot, A M. Thorndike and A. M. Wetherell, Phys. Letters 28B (1968) 67.
[27] T. Lasinski, R. Levi Setti and E. Predazzi, Phys. Rev. 179 (1969) 1426.
[28] A D Krisch, Phys. Rev. Letters 19 (1967) 1149.